International Journal of
Automotive Manufacturing and Materials（IJAMM）

Article

Laminar Burning Velocity of $NH_3/CH_4/H_2/CO_2$/Air Premixed Flames under Elevated Temperatures and Pressures: An Experimental and Kinetic Study

Wenchao Zhu [1], Xiangyu Meng [1,*], Zechuan Cui [2], Jiangping Tian [2], and Wuqiang Long [2]

[1] School of Chemical Engineering, Dalian University of Technology, Dalian 116024, China
[2] Institute of Internal Combustion Engine, Dalian University of Technology, Dalian 116024, China
* Correspondence: mengxiangyu@dlut.edu.cn

Received: 8 July 2025; Revised: 5 August 2025; Accepted: 12 August 2025; Published: 14 August 2025

Abstract: Blending with methane (CH_4) considerably enhances the reactivity of pure ammonia (NH_3) during co-firing. The partial cracking of NH_3 produces hydrogen (H_2), which further improves combustion efficiency. Additionally, the addition of carbon dioxide (CO_2) helps significantly reduce nitrogen oxide (NOx) emissions. However, fundamental experimental data on the laminar combustion characteristics of $NH_3/CH_4/H_2/CO_2$/air flames are scarce, especially under elevated temperatures and pressures. In this work, laminar burning velocities (LBV) of $NH_3/CH_4/H_2/CO_2$/air premixed flames were measured in a constant volume combustion chamber (CVCC) at different CO_2 additions (X_{CO2} = 0%, 10% and 30%), fuel compositions (40/40/20 and 30/30/40 $NH_3/CH_4/H_2$) at 500 K and 5 atm. The results indicated that CO_2 dilution suppresses the formation of surface wrinkles on the flame, whereas excessive dilution leads to an upward shift of the flame center. The inhibitory effect of CO_2 on the LBV is primarily attributed to the dilution-induced reduction in the concentrations of O, H, and OH radicals, followed by thermal effects. As the CO_2 dilution ratio and equivalence ratio increase, the reverse direction of reaction R21 ($CO + OH = CO_2 + H$) is significantly enhanced. This reaction competes with R1 ($H + O_2 = O + OH$) for H radicals, thereby effectively suppressing flame propagation. Moreover, when the CO_2 dilution ratio increases from 0% to 50%, NO emissions decrease significantly. The proportion of thermal + prompt NO decreases from approximately 10% to below 2%, mainly due to the substantial decrease in adiabatic flame temperature.

Keywords: ammonia/methane/hydrogen; CO_2 dilution; laminar burning velocity; NO emission; chemical kinetics

1. Introduction

To achieve the global temperature control targets established by the Paris Agreement, countries around the world are intensifying efforts to reduce greenhouse gas emissions [1 – 3]. In 2023, the International Maritime Organization set a carbon-reduction goal for shipping, mandating at least a 70% reduction in CO_2 emissions by 2025 relative to 2008 levels [4]. Among emerging carbon-neutral energy carriers [5 – 7], ammonia (NH_3) has attracted considerable attention due to its high hydrogen (H_2) content, ease of storage and transportation, and carbon-free combustion characteristics [8, 9]. Compared with H_2, NH_3 is significantly easier to store, as it can be liquefied at a pressure of only 0.8 to 1.0 MPa. It can also be transported using existing infrastructure, making it a strong candidate for large-scale applications in power generation, marine propulsion, and industrial heating [10]. As a carbon-free fuel, ammonia does not produce direct CO_2 emissions during combustion. In addition, it can be synthesized from renewable electricity through green hydrogen pathways, enabling a fully decarbonized energy cycle [11]. At present, the global maritime industry is actively exploring NH_3-fuelled engine systems to meet international decarbonization targets. However, the practical application of NH_3 still faces several challenges, including low reactivity, high ignition temperature, and the potential formation of nitrogen-based pollutants such as nitrogen oxides (NO_x). Therefore, further research is urgently needed to improve combustion performance and control emissions.

Blending NH_3 with high-reactivity fuels, such as H_2, methane (CH_4) [12,13], methanol (CH_3OH) [14,15], and dimethyl ether (DME) [16], is widely recognized as an effective strategy to enhance its combustion performance. These additives help to overcome the low laminar burning velocity (LBV) and high ignition temperature associated with NH_3 by promoting radical generation and heat release during combustion. In recent years, research on NH_3 blended with multi-component fuels has gradually emerged. Yu et al. [17] investigated the combustion characteristics of NH_3 blended with H_2 and DME using a constant-volume combustion chamber (CVCC). Their results showed that the addition of DME or H_2 primarily plays an ignition-promoting or flame-accelerating role, respectively, thereby increasing the LBV. Li et al. [18] found through experiments and kinetic analysis that the LBV of NH_3/DME/air mixtures increases with the addition of H_2. However, the growth rate decreases as the NH_3/DME blend ratio becomes higher. Berwal et al. [19] employed an externally heated diverging channel technique to measure the LBV of $CH_4/H_2/NH_3$ blends at high temperatures, and found that under a CH_4 to H_2 ratio of 4 to 1, blending 0 to 30% NH_3 yields LBV and adiabatic flame temperature values (Tad) comparable to those of pure CH_4. Yasiry et al. [20] pointed out that $CH_4/H_2/NH_3$ blends can be considered suitable alternatives to conventional fuels in industrial applications. They noted that increasing the LBV requires shifting the mixture composition toward higher concentrations of CH_4 and H_2 and lower concentrations of NH_3. Chu et al. [21] used a shock tube to measure the ignition delay time of $NH_3/H_2/CH_4$ ternary fuels. The results showed that changing the H_2/CH_4 ratio causes the ignition delay time curve to shift vertically. Increasing the H_2/CH_4 ratio significantly raises the upper limit of the ignition-promoting effect.

Recycling CO_2-enriched flue gas as part of the exhaust gas recirculation [22] strategy effectively reduces the flame temperature during NH_3 combustion and modifies the dominant reaction pathways, which contributes to the suppression of NO_x formation. Chen et al. [23] investigated the conversion characteristics of fuel-N during ammonia/coal blends in a CO_2 atmosphere using a high-temperature furnace. The experimental results indicated that compared to an N_2 atmosphere, CO_2 suppresses NO formation during co-combustion. However, the inhibitory effect of CO_2 on NO generation per unit mass gradually weakens as the temperature increases. Czyzewski et al. [24] analyzed flameless combustion of $NH_3/H_2/CH_4$ blended fuels under CO_2-diluted conditions. They reported that the conversion of ammonia to NO follows a nonlinear trend and decreases as the CO_2 content in the fuel increases. However, under conditions of high equivalence ratio (ER) and CO_2 concentration, the NO content in the exhaust gas increases. Gao et al. [25] conducted kinetic analysis to evaluate the mechanisms by which CO_2 addition influences NO formation during NH_3/CH_3OH combustion, and found that the presence of CO_2 suppresses NO generation based on thermal effects. Alzueta et al. [26] examined the conversion behavior of NH_3 and NH_3/NO mixtures in a CO_2 atmosphere. The presence of NO in the NH_3/CO_2 reaction system promotes the conversion of NH_3 under fuel-rich conditions, while it delays the onset of the conversion process.

Blending with CH_4 considerably enhances the reactivity of pure NH_3 during co-firing. Partial cracking of NH_3 can convert NH_3/CH_4 to $NH_3/CH_4/H_2$ blends. Additionally, CO_2, added as a dilution gas into the fuel-air blend, can effectively decrease NO_x emissions by reducing the flame temperature. Currently, research on the LBV of $NH_3/CH_4/H_2$/air premixed flames has gained significant attention globally [19,20,27]. Thus, exploring the effect of CO_2 on the LBV of $NH_3/CH_4/H_2$/air premixed flames under elevated temperatures and pressures is essential for understanding its potential effects on flame behavior and emissions. In this study, the LBV was measured by a constant volume combustion chamber (CVCC) at different CO_2 additions (X_{CO2} = 0%, 10% and 30%), fuel compositions (40/40/20 and 30/30/40 $NH_3/CH_4/H_2$) at 500 K and 5 atm. This research expands the experimental database and analyzes the flame propagation. Furthermore, a detailed chemical kinetic analysis was conducted based on a previously developed $NH_3/CH_4/H_2$/CO reaction kinetic mechanism [28] to gain insight into the combustion and emissions process of $NH_3/CH_4/H_2/CO_2$/air premixed flames.

2. Methods

2.1. Experimental Methods

The constant volume combustion chamber (CVCC) experimental setup is illustrated in Figure 1. It consists of a CVCC, a heating system, an ignition system, an intake system, an imaging system, and a control and data acquisition system. The actual structure of the CVCC is shown in Figure 2. It has a volume of 1.44 L and an aspect ratio of 1.525. Both sides are equipped with optical visualization windows with a diameter of 100 mm. An externally wrapped annular heating design was adopted to ensure uniformity and stability of the internal temperature field. The maximum heating temperature is 900 K, and the pressure resistance reaches up to 4 MPa. To further reduce the temperature gradient inside the CVCC, a temperature controller and K-type thermocouples were used to regulate the heating process. The chamber was first heated to a temperature 5–12 K above the target, and ignition was initiated once the temperature decreased to the target. The ignition system consists of two rod electrodes with a diameter of 0.7 mm. One electrode was connected to a spark plug that served as the ignition terminal, while the other functioned as the grounding terminal. The spark plug was mounted at the top of the chamber using a dedicated adapter to ensure its stability and precise positioning. The gap between the electrodes was maintained at approximately 2 mm.

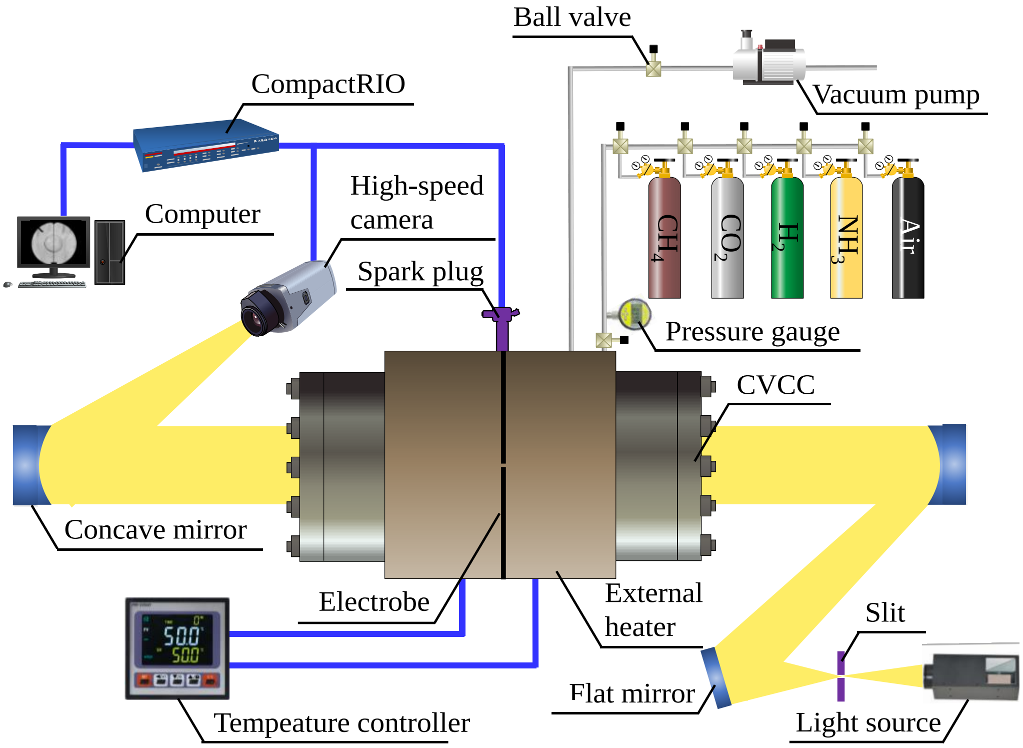

Figure 1. Experimental setup.

Figure 2. Actual diagram of the CVCC experimental setup.

Before preparing the gas mixture, the CVCC was evacuated using a vacuum pump. According to Dalton's law of partial pressures, gases were introduced sequentially into the chamber: a portion of air was added first, followed by NH_3, CH_4, H_2, and CO_2. Finally, additional air was injected to reach the target pressure. Throughout this process, a pressure gauge with an accuracy of ±0.005 MPa was used for monitoring. All gases used in the experiments had a purity greater than 99.99%, and the air was composed of 79% N_2 and 21% O_2. A Z-shaped optical path coupled with a high-speed camera was used to capture flame images. High-speed images were acquired using a Photron FASTCAM SA-Z camera (Photron, Tokyo, Japan), which supports a maximum resolution of 1024 × 1024 pixels and frame rates up to 20,000 fps. To improve image quality, a Nikon AF-S VR 70–300 mm f/4.5–5.6 G IF-ED lens (Nikon Corporation, Tokyo, Japan) was employed, offering an adjustable aperture range from f/4.5 to f/40, a focal-length range of 70–300 mm, and a minimum focusing distance of 1.5 m. The ignition process and high-speed camera were precisely triggered using the CompactRIO data acquisition and control module, ensuring synchronization between imaging and ignition, and each experimental condition was tested at least three times to ensure accuracy and repeatability.

The initial temperature (T_0) and pressure (P_0) were set to 500 K and 5 atm, respectively. The equivalence ratio (ER) ranged from 0.6 to 1.3, and the oxidizer was air. This study investigated the influence of CO_2 dilution, achieved by adding different mole fractions to the fuel, on the laminar combustion characteristics of $NH_3/CH_4/H_2$. The mole fraction of each component in the fuel was calculated using Equation (1).

$$X_i = (1 - X_{CO_2}) \times \frac{V_i}{V_{H_2} + V_{CH_4} + V_{NH_3}} \tag{1}$$

Where X_i and V_i are the mole fraction and volume fraction of each component, respectively. Table 1 shows the experimental conditions.

Table 1. The experimental conditions.

T_0 (K)	P_0 (atm)	Φ	$V_{NH3}/V_{CH4}/V_{H2}$ (%)	X_{CO2} (%)	X_{CO2}:X_{NH3}:X_{CH4}:X_{H2} (%)
500	5	0.6–1.3	40%/40%/20%	0%	0:40:40:20
				10%	10:36:36:18
				30%	30:28:28:14
			30%/30%/40%	10%	10:27:27:36
				30%	30:21:21:28

2.2. Data Processing

The flame propagation images were processed using a MATLAB program to extract the variation of flame radius over time, from which the stretched flame speed (S_b) was calculated using Equation (2):

$$S_b = \frac{dR_f}{dt} \tag{2}$$

where R_f and t represent the flame radius and time, respectively. For a spherical flame, the stretch rate was calculated using Equation (3):

$$\varepsilon = \frac{1}{R_f} S_b \tag{3}$$

The unstretched flame speed (S_b^0) was obtained by extrapolating the stretched flame speed. The linear model [29] is not applied under large stretch rates. Instead, a nonlinear model proposed by Frankel et al. [30] was adopted in this study, as shown in Equation (4):

$$S_b = S_b^0 - S_b^0 \frac{2L_b}{R_f} \tag{4}$$

where L_b is the Markstein length. Finally, the laminar burning velocity (S_L) of the unburned gas was calculated based on the law of mass conservation, as shown in Equation (5):

$$A\rho_u S_L = A\rho_b S_b^0 \tag{5}$$

where ρ_u and ρ_b are the densities of burned and unburned gases, respectively.

Figure 3a shows the flame radius as a function of time for a mixture of 40% NH_3 + 40% CH_4 + 20% H_2 under conditions of an ER of 1.3 and 10% CO_2 dilution at 500 K and 5 atm. The results of the three repeated experiments exhibit good consistency. Numerous studies [31, 32] have shown that when the flame radius exceeds 6 mm, the influence of the ignition electrodes becomes negligible. In addition, when the flame radius exceeds 28 mm, the stretched flame speed varies rapidly with the stretch rate due to limitations of the CVCC geometry and the presence of flame instabilities. Therefore, to avoid the ignition effects in the initial stage, and the influence of flame instabilities and buoyancy effects in the later stage, data points in the quasi-steady region with flame radii ranging from 6 to 25 mm were selected for calculating LBV. This flame radius range has been widely adopted in literature [33–35]. Figure 3b illustrates that the nonlinear model can accurately determine the stretched flame speed under various initial ER, and $R^2 > 0.99$, indicating that this model is suitable for calculating the LBV under different initial conditions.

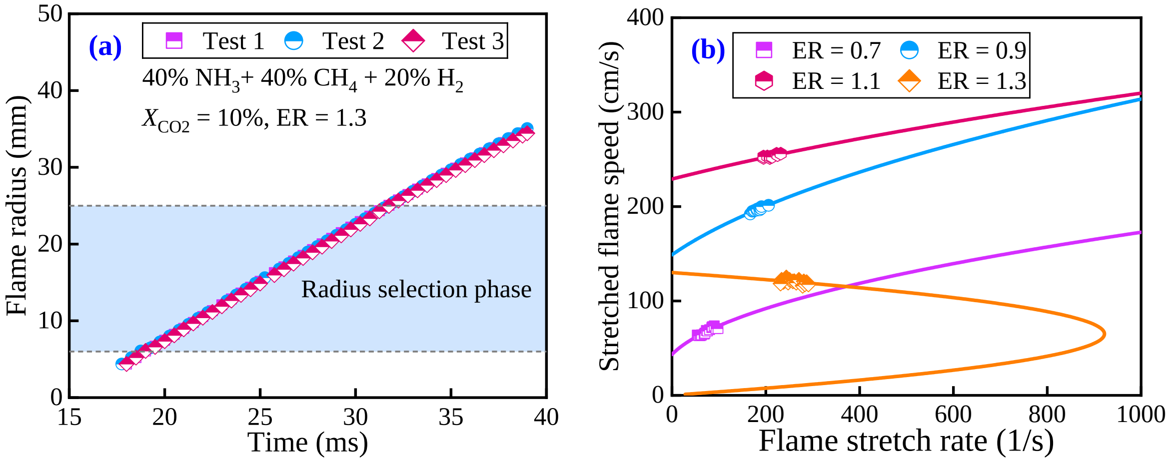

Figure 3. (**a**) Flame radius versus time curve, and (**b**) extrapolation results of nonlinear model (40% NH_3 + 40% CH_4 + 20% H_2, X_{CO2} = 10%, T_0 = 500 K, and P_0 = 5 atm).

2.3. Uncertainty Analysis

The experimental uncertainty primarily originated from factors such as sensor accuracy, measurement repeatability, and variations in environmental conditions during the testing process [36]. In addition, the radiative effect of the spherical flame could also influence the calculation of the LBV [37]. Therefore, the overall uncertainty (u_C) of the LBV was calculated using Equation (6):

$$u_C = \sqrt{u_R^2 + u_S^2 + u_r^2} \tag{6}$$

Where u_R is random uncertainty, and it was calculated using Equation (7):

$$u_R = t_{N-1.95} \cdot \frac{S_R}{\sqrt{N}} \tag{7}$$

Where S_R denotes the standard deviation of LBV, N is the number of repeated experiments, and $t_{N-1.95}$ is the student-*t* distribution coefficient corresponding to a 95% confidence level with $N-1$ degrees of freedom.

The u_S is systematic uncertainty. The uncertainties associated with the pressure gauge and *K*-type thermocouple are ±0.4% and ±0.75%, respectively. Within a narrow range, the influence of temperature and pressure on the LBV can be assumed to follow a linear relationship. Therefore, the uncertainties in the accuracy of the pressure gauge and the K-type thermocouple can be regarded as systematic errors introduced by the measurement system.

The u_r is the uncertainty caused by flame radiation, and it was calculated using Equation (8):

$$u_r = 0.82 S_L \left(\frac{S_L}{S_0}\right)^{-1.44} \left(\frac{T_0}{T_{298\ \mathrm{K}}}\right)\left(\frac{P_0}{P_{0.1\ \mathrm{MPa}}}\right)^{-0.2} \tag{8}$$

Where S_0 = 1 cm/s. For each set of experiments, the LBV was averaged after at least three measurements were performed and outliers were excluded, to ensure the stability and reliability of the data. Finally, the maximum experimental uncertainty in this study is 7.89%, the minimum uncertainty is 0.33%, and the average uncertainty is 4.70%. The uncertainties in the experimental results of LBV were presented in the form of error bars.

2.4. Numerical Methods

Cantera was used to calculate the LBV of a steady one-dimensional freely propagating premixed flame. A multicomponent transport model was adopted, and the Soret effect was included. To ensure numerical reliability, the computational domain was extended to 10 cm, and the adaptive refinement criteria for gradient and curvature were set to 0.06 and 0.12, respectively, yielding a converged solution on more than 500 grid points. The adiabatic flame temperature (T_{ad}) was calculated via the chemical equilibrium and phase-equilibrium module. In this study, five chemical kinetic mechanisms were employed, including our group-Mech [28], Okafor-Mech [13], Shrestha-Mech [38], Zhou-Mech [39], and Wang-Mech [40]. Our group-Mech [28] is a previously developed combustion kinetics of $NH_3/CH_4/H_2/CO$ blends. It consists of 53 species and 353 reactions, and it can be extensively validated for NH_3, H_2, CH_4, CO, and their blends. This mechanism accurately predicts LBV over a temperature range of 298 to 750 K, a pressure range of 1 to 15 atm, and ERs from 0.6 to 1.7. It also reproduces ignition delay times within the range of 860 to 2000 K, 1.2 to 40 atm, and ERs from 0.3 to 2.0. Furthermore, it is capable of predicting species distributions in burner-stabilized flames, plug flow reactors, and jet-stirred reactors across a wide range of conditions, especially for NO_x and N_2O emissions.

Figure 4 shows a comparison between the simulation results of five mechanisms and the current experimental data on LBV for different initial conditions. Compared to the experimental results, Okafor-Mech [13] significantly underpredicts LBV, while Shrestha-Mech [38] overpredicts it. Zhou-Mech [39] and Wang-Mech [40] show improved accuracy. However, both tend to slightly overpredict LBV under lean and stoichiometric conditions. The mechanism developed for $NH_3/CH_4/H_2/CO$ blends by our group [28] successfully reproduces the experimental LBV values under various initial conditions. Therefore, our group-Mech [40] was selected for the subsequent kinetic simulations.

To further analyze the effect of CO_2 dilution on flame propagation, the virtual gas method [41] was used to comprehensively quantify the dilution, chemical, transport, and thermal effects on LBV. Specifically, two inert surrogate diluents were introduced. FCO_2 shares identical thermodynamic and transport properties with CO_2. FCO_2* matches CO_2 in thermodynamic properties and replicates N_2 in transport properties. The chemical contribution was quantified by the LBV difference between CO_2 and FCO_2 cases. The transport contribution was determined by the LBV difference between FCO_2 and FCO_2* cases. The thermal contribution was assessed by the LBV difference between FCO_2* and N_2 cases. Contribution factors for each mechanism were calculated using the appropriate formulae to quantify their impact on LBV.

$$\begin{aligned}
CF_{\text{Dilution}} &= \frac{S_L(\text{Non}-\text{diluted}) - S_L(\mathrm{N_2})}{S_L(\text{Non}-\text{diluted}) - S_L(\mathrm{CO_2})} \\
CF_{\text{Thermal}} &= \frac{S_L(\mathrm{N_2}) - S_L(\mathrm{FCO_2^*})}{S_L(\text{Non}-\text{diluted}) - S_L(\mathrm{CO_2})} \\
CF_{\text{Transport}} &= \frac{S_L(\mathrm{FCO_2^*}) - S_L(\mathrm{FCO_2})}{S_L(\text{Non}-\text{diluted}) - S_L(\mathrm{CO_2})} \\
CF_{\text{Chemical}} &= \frac{S_L(\mathrm{FCO_2}) - S_L(\mathrm{CO_2})}{S_L(\text{Non}-\text{diluted}) - S_L(\mathrm{CO_2})}
\end{aligned} \tag{9}$$

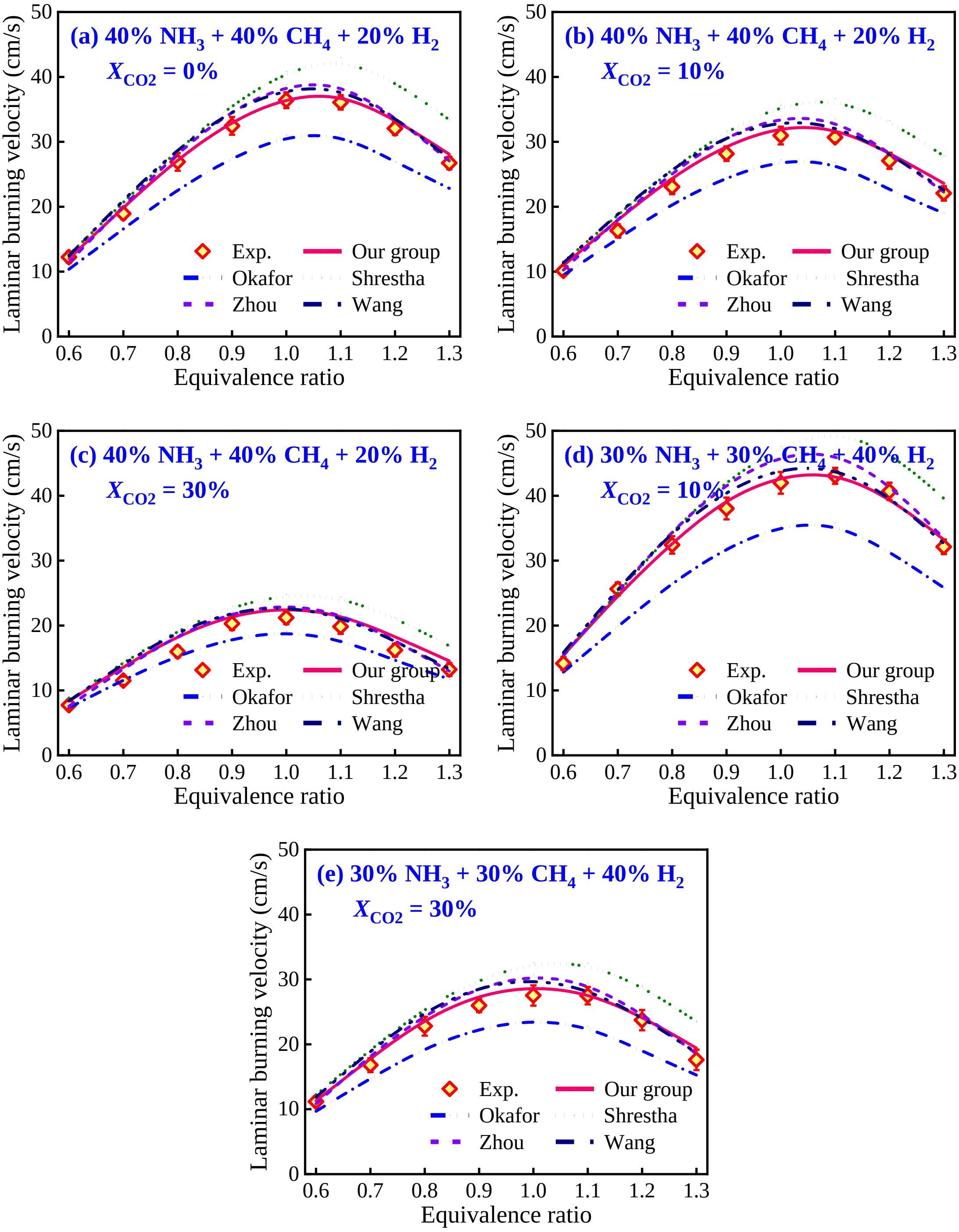

Figure 4. Comparison between the simulation results of LBV for different initial conditions (T_0 = 500 K, P_0 = 5 atm).

Previous studies [42,43] used isotope labeling to distinguish NO_x produced from NH_3 combustion (i.e., fuel NO_x) and oxidation of N_2 in air, where N* denotes nitrogen sources from N_2 in air (i.e., thermal + prompt NO_x). In this study, the approach was further extended based on the work of Li et al. [44]. Various N-containing species with rotationally asymmetric structures were considered, and the position of each N atom was explicitly identified. Specifically, rotationally asymmetric species such as N_2O can be classified into four labeled variants: N_2O, N*NO, NN*O, and N*N*O. Rotationally symmetric species such as N_2H_2 can be classified into three labeled variants: N_2H_2, N*HNH, and N*HN*H. This method ensures that the isotope-labeled mechanism can better reproduce simulation results consistent with the original mechanism. The previously developed $NH_3/H_2/CH_4/CO$ kinetics mechanism [28] was expanded from 53 species and 353 reactions to include 84 species and 756 reactions using the improved isotope labeling method. To validate this method, Figure 5 shows the variations of NO_x and N_2O during combustion under one-dimensional laminar flame conditions. One corresponds to the original mechanism without isotope labeling, and the other to the modified mechanism with isotope labeling. The results from both mechanisms under the same conditions exhibit a high degree of similarity. Specifically, under laminar flame conditions, the maximum relative error is only 0.75%. This demonstrates that the modified isotope labeling method can accurately and effectively identify the generation processes of NO_x produced from NH_3 combustion and N_2 oxidation.

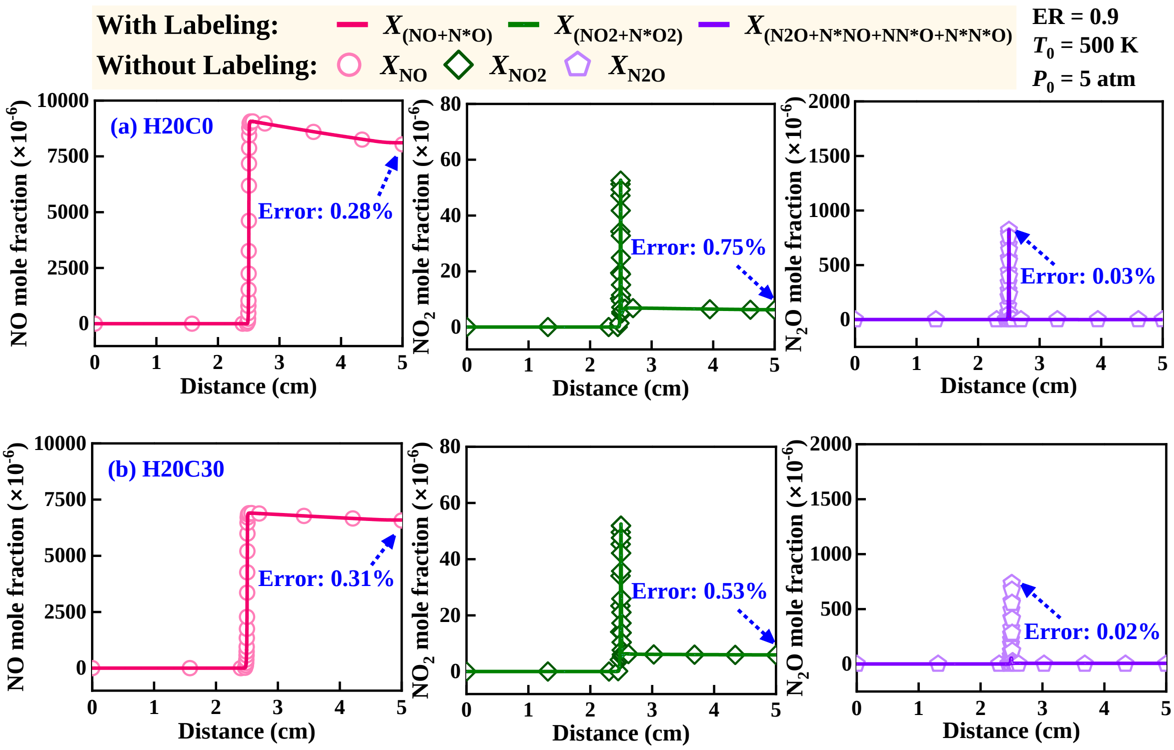

Figure 5. Validation of the modified isotope labeling method for varying CO_2 dilution ratios (40%NH_3 + 40%CH_4 + 20%H_2, ER = 0.9, T_0 = 500 K, and P_0 = 5 atm).

3. Results and Discussion

3.1. Effect on CO_2 Dilution and Equivalence Ratio on the Combustion Characteristics

Figure 6 shows the flame development images of 40%NH_3 + 40%CH_4 + 20%H_2 with varying CO_2 dilution ratios at an ER of 1.0. During the ignition process, interference from the electrodes caused slight wrinkling of the flame along the electrode axis, while other regions of the flame remained relatively smooth. Because the mixture contained a high proportion of H_2 and CH_4, no significant buoyancy effect, such as that caused by the slow LBV in pure NH_3 combustion [45], appears under any condition. As the CO_2 dilution ratio increases, the cracks and cellular structures on the flame surface gradually weaken. However, excessive CO_2 prevents the formation of a fully spherical flame. These results indicate that an appropriate amount of CO_2 dilution helps maintain relatively high flame propagation speed and improves flame stability.

Figure 7 shows the fuel composition of NH_3, CH_4, and H_2 at simulated LBVs of 20, 25, and 30 cm/s for varying CO_2 dilution ratios and ERs. The composition of the blended fuel at any constant LBV tends to shift towards the upper right region of the ternary plot, indicating an increase in NH_3 and H_2 content and a decrease in CH_4 content. For example, in Figure 7a, when 30% CO_2 is added, maintaining a constant LBV of 30 cm/s requires increasing the H_2 content from 0 to 40% and the NH_3 content from 14% to 28%, while the CH_4 content decreases from 56% to 0. Figure 7a also shows that CO_2 dilution reduces LBV, which necessitates a higher H_2 content to compensate. In addition, an increase in LBV causes the fuel composition to shift towards the lower right region of the ternary plot, where the mixture contains more H_2 and CH_4 and less NH_3. Figure 7b shows that cases with ERs of 0.7 and 1.3 shift further towards the lower right compared to the case with an ER of 1.0, with the shift being more pronounced when the ER is 0.7.

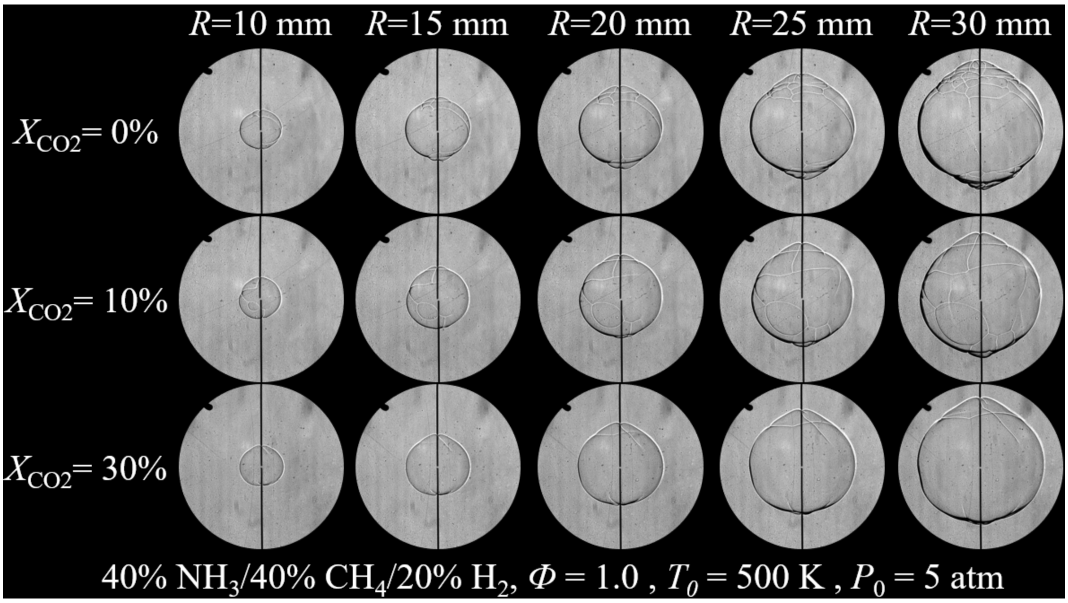

Figure 6. Flame development images with varying CO_2 dilution ratios.

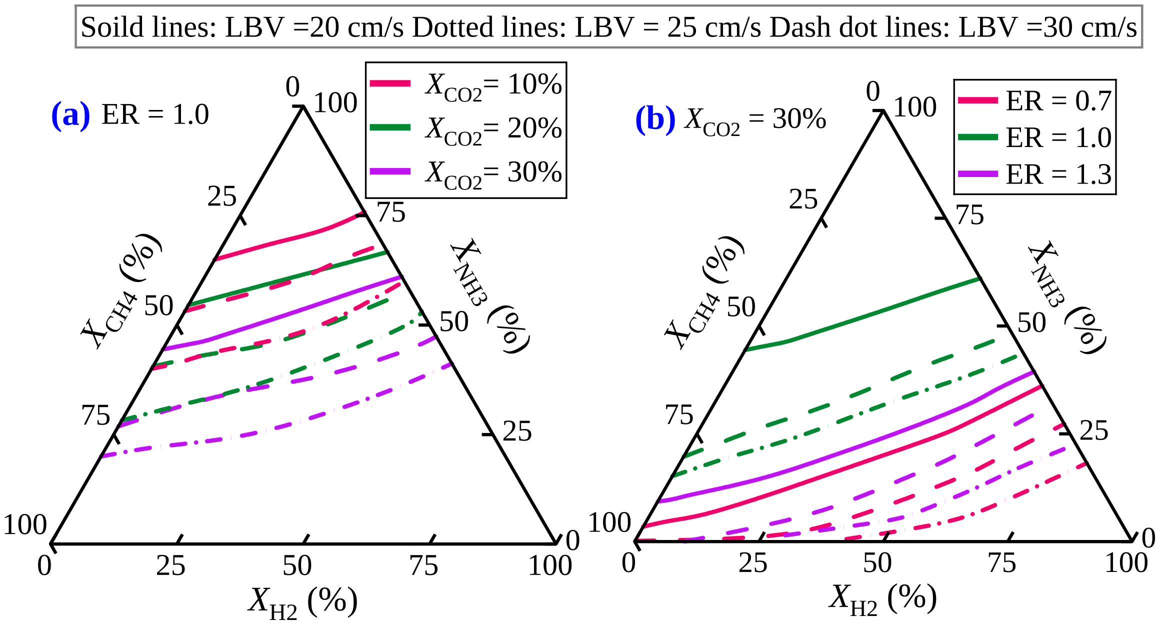

Figure 7. Simulated LBV values of $NH_3/CH_4/H_2/CO_2$/air flames constant at 20, 25 and 30 cm/s for varying CO_2 dilution ratios and ERs (T_0 = 500 K, P_0 = 5 atm).

As shown in Figure 8, the effects of varying CO_2 dilution ratios and ERs on LBV are decoupled. Figure 8a shows that the dilution effect plays a dominant role in reducing LBV, contributing to more than 42.6% of the total LBV reduction. Moreover, the thermal and chemical effects also play significant roles, while the transport effect is negligible. As the CO_2 dilution ratio increases, the contribution of the dilution effect shows a monotonic increasing trend, whereas that of the chemical effect demonstrates an opposite trend. Meanwhile, the contributions of thermal and transport effects are virtually unaffected. This suggests that the inhibition of LBV by CO_2 depends more on the dilution effect at high dilution concentrations. Figure 8b shows that the dilution effect decreases and then increases with increasing ERs for a fixed CO_2 dilution ratio, whereas the chemical effect increases and then decreases. This is attributed to the heat release rate and chemical reaction rate being lower than at the stoichiometric ratio under both lean-burn and rich-burn conditions [46]. Furthermore, as the ER increases, the contribution of the thermal effect continually decreases, indicating that LBV is more sensitive to the temperature variations caused by the CO_2 dilution under lean-burn conditions.

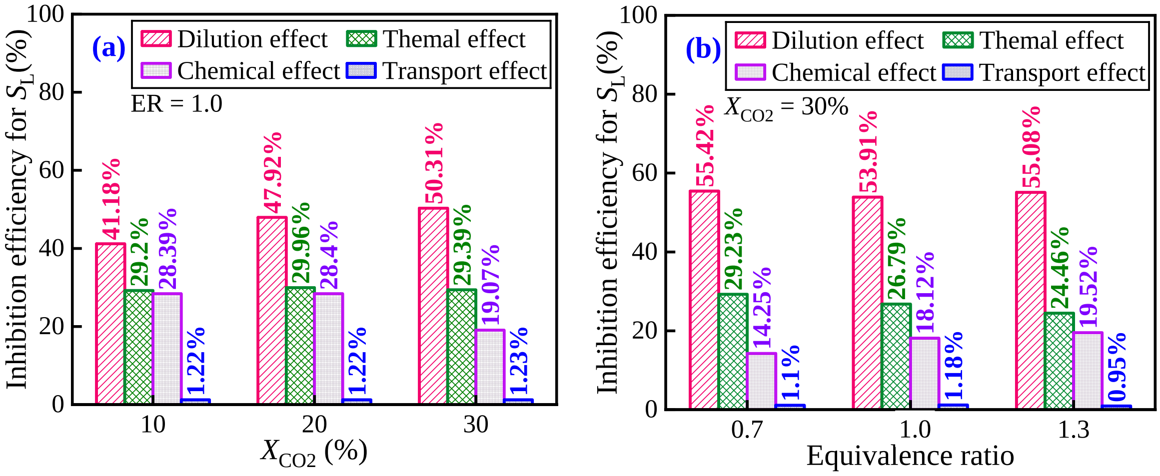

Figure 8. Decoupling of the effects on LBV for varying (**a**) CO_2 dilution ratios and (**b**) ERs (40% NH_3 + 40% CH_4 + 20% H_2, T_0 = 500 K, and P_0 = 5 atm).

The maximum O + H + OH radical concentration ($(O + H + OH)_{max}$) and adiabatic flame temperature (T_{ad}) are closely related to variations in LBV. Figure 9 presents the relative reductions in T_{ad} and $(O + H + OH)_{max}$ for different CO_2 dilution ratios and ERs. The thermal effect was represented by FN_2-FCO_2, which characterizes the decrease in T_{ad} and $(O + H + OH)_{max}$ solely due to the endothermic nature of CO_2. Additionally, the influence of transport effects is negligible and thus not considered. The results indicate that the relative reductions in both T_{ad} and $(O + H + OH)_{max}$ exhibit a continuous decreasing trend with rising CO_2 dilution ratios, which is exacerbated by increasing ERs. Furthermore, it is found that the dilution effect of CO_2 played a dominant role in reducing T_{ad} and $(O + H+ OH)_{max}$, followed by the thermal effect, while the chemical effect had the minimal impact, which is consistent with the decreasing trend of LBV shown in Figure 9. However, the maximum reduction in T_{ad} due to the dilution effect is only 4.4%, whereas the maximum reduction in $(O + H + OH)_{max}$ can reach up to 40%. This indicates that the decrease in $(O + H + OH)_{max}$ resulting from the CO_2 dilution effect is the main reason for the inhibition of LBV, particularly under rich-burn conditions.

Figure 10 presents the sensitivity analyses of LBV at different CO_2/FCO_2 dilution ratios and ERs. The results reveal that the reactions affecting LBV mainly involve O, H, and OH radicals. R1 ($H + O_2 = OH + O$) is the most critical reaction enhancing LBV under all conditions, with its sensitivity coefficient increasing as CO_2 dilution ratios and ERs. rise. The reaction with the highest negative sensitivity coefficient shifts from R5 ($H + O_2(+M) = HO_2(+M)$) at an ER of 0.7 to R70 ($H + CH_3(+M) = CH_4(+M)$) at ERs of 1.0 and 1.3. The number and importance of CH_4-related reactions increase. Additionally, NH_3-related reactions, which contain only R179 ($NH_2 + O = HNO + H$) and R193 ($NH_2 + NO = NNH + OH$), have a minor effect on LBV. This indicates that $NH_3/CH_4/H_2/CO_2$/air flames are primarily driven by H_2 chemistry under lean-burn conditions, gradually transitioning to CH_4 chemistry under rich-burn conditions.

Previous studies [41,47] have indicated that R21 ($CO + OH = CO_2 + H$) is the most critical reaction involving CO_2. As shown in Figure 10, the sensitivity coefficient of R21 gradually decreases with increasing CO_2 dilution ratios and ERs. This trend not only reflects the diminished importance of R21 itself to LBV but also suggests an intensification of its reverse reaction. The competition with R1 for H radicals improves the importance of other H radical-related reactions to LBV. Furthermore, compared to a CO_2 dilution ratio of 30%, the absolute values of the sensitivity coefficients for reactions primarily involving O, H, and OH radicals show little decrease at a FCO_2 dilution ratio of 30%. This indicates that the chemical effect of CO_2 dilution has a relatively limited impact on $NH_3/CH_4/H_2$/air flames.

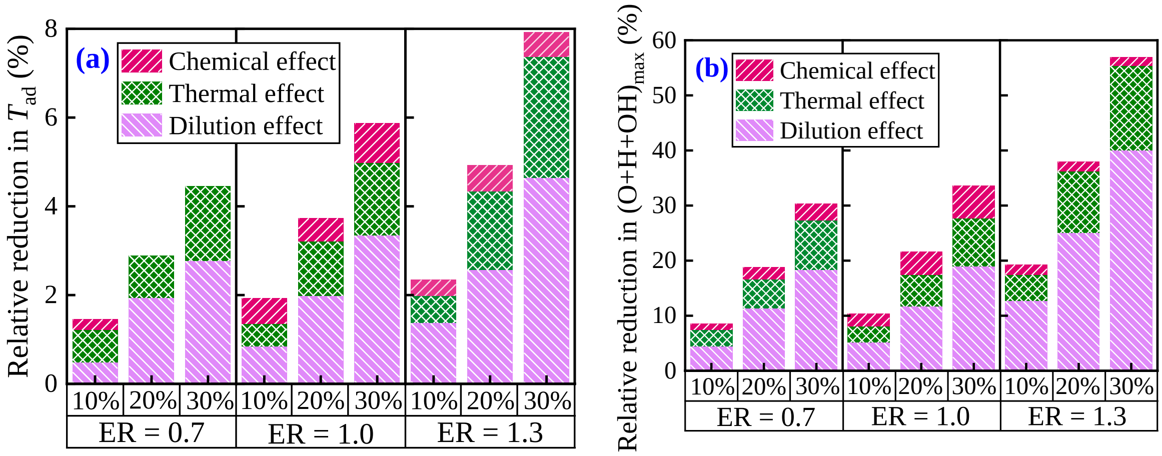

Figure 9. Relative reductions in (**a**) T_{ad} and (**b**) $(O + H + OH)_{max}$ for varying CO_2 dilution ratios and ERs (40% NH_3 + 40% CH_4 + 20% H_2, T_0 = 500 K, and P_0 = 5 atm).

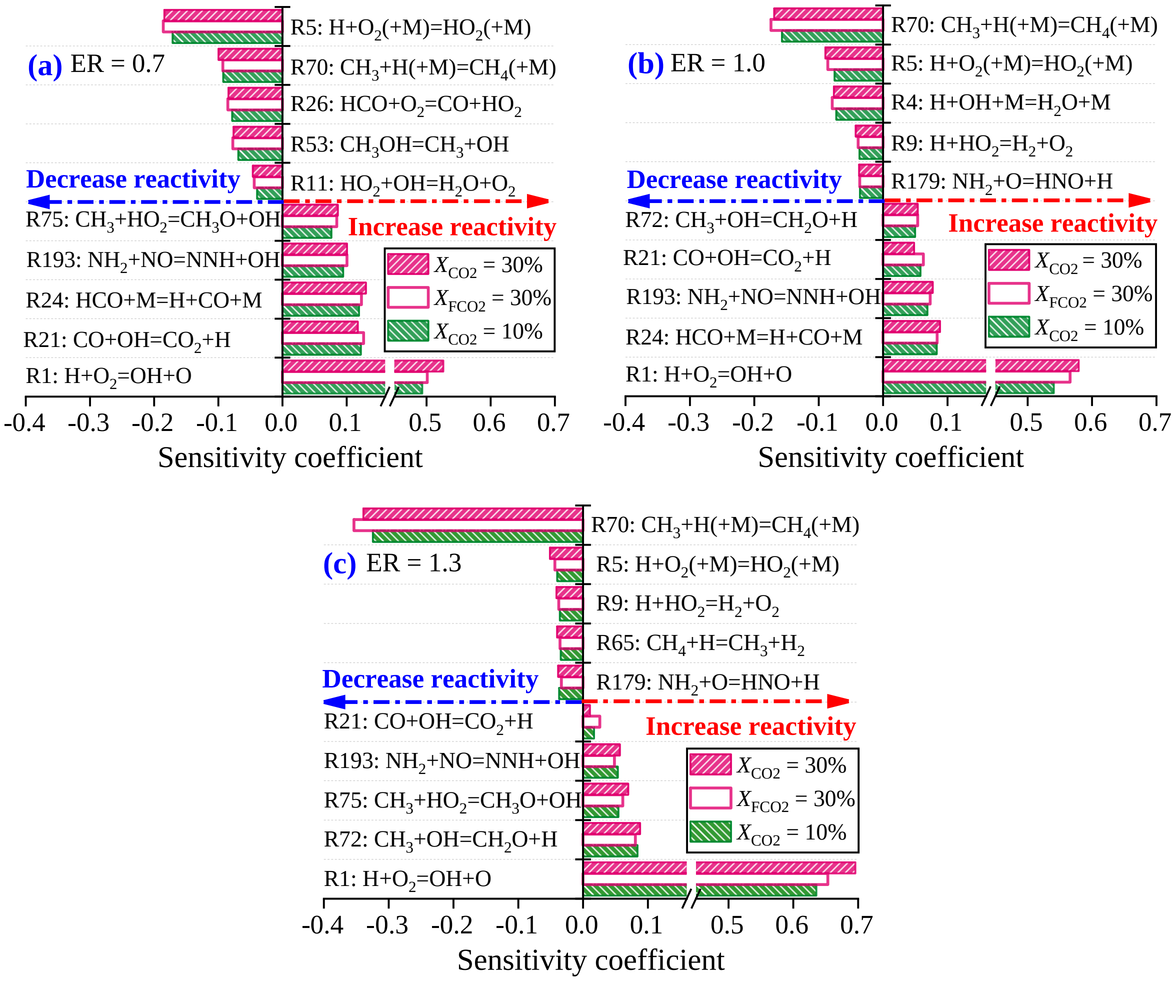

Figure 10. Sensitivity analyses of LBV for varying FCO_2/CO_2 dilution ratios and ERs (40% NH_3 + 40% CH_4 + 20% H_2, T_0 = 500 K, and P_0 = 5 atm).

3.2. Effect on CO_2 Dilution and Equivalence Ratio on the NO Emissions

Figure 11 shows the variation in final NO mole fraction for CO_2 dilution ratios and ERs. The results indicate that NO emissions first increase and then decrease with increasing ER, reaching a peak near an ER of 0.9 under all CO_2 dilution conditions. At a fixed ER, increasing the CO_2 dilution ratio leads to a reduction in NO emissions. This reduction is more significant when the CO_2 dilution increases from 30% to 50%, compared to the range from 10% to 30%. This is because increasing the CO_2 dilution from 30% to 50% results in a greater decrease in T_{ad} and radical concentrations. When using the NO emissions from pure NH_3 at ERs of 0.9 and 1.0 as baselines under the same initial conditions, it is observed that although CO_2 dilution reduces the overall energy density of the reactants, the presence of H_2 and CH_4 still promotes higher NO formation. Only when the ER exceeds 1.2 can the NO emission be reduced below the level observed in pure NH_3.

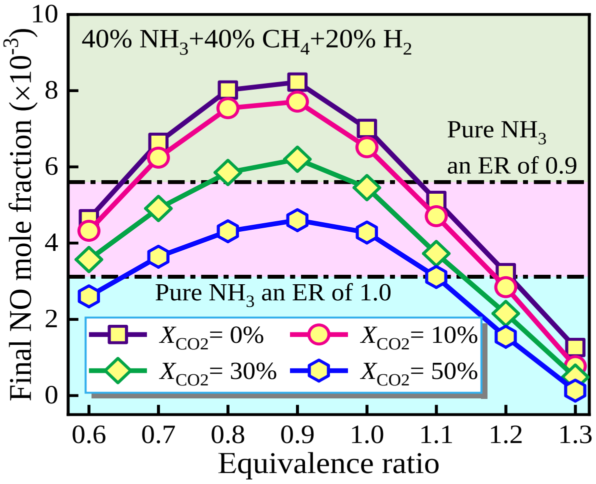

Figure 11. Variation in final NO mole fraction for CO_2 dilution ratios and ERs (40% NH_3 + 40% CH_4 + 20% H_2, T_0 = 500 K, and P_0 = 5 atm).

Figure 12 shows the effect of different CO_2 dilution ratios on the rate of production (ROP) of key elementary reactions involved in NO formation and consumption during combustion at an ER of 0.9. For ease of comparison, the ROP values for both NO formation and consumption reactions are plotted using the same vertical axis scale. The results indicate that as the CO_2 dilution ratio increases, the ROP of both NO formation and consumption reactions gradually decreases, and the timing of these reactions shifts to later stages. Among all reactions, the formation of NO is most strongly influenced by the HNO radical. In particular, reaction R222 ($HNO + H = H_2 + NO$) remains the dominant pathway for NO formation under all conditions. Since this reaction is highly temperature-sensitive, the reduction in flame temperature caused by increased CO_2 dilution leads to a more pronounced decrease in its ROP compared to other reactions. In addition, the presence of CH_4 enhances the contribution of reaction R314 ($HNO + CH_3 = CH_4 + NO$) to NO formation. On the other hand, NO consumption primarily occurs through reactions with NH and NH_2 radicals, including reaction R2O4 ($NO + NH = H + N_2O$), reaction R193 ($NO + NH_2 = OH + NNH$), and reaction R192 ($NO + NH_2 = H_2O + N_2$).

Figure 13 shows the variation in different NO formation sources and T_{ad} under various CO_2 dilution ratios at an ER of 0.9. It is observed that under non-diluted conditions, thermal + prompt NO accounts for approximately 10% of the total NO. However, as the CO_2 dilution ratio increases, the proportion of thermal + prompt NO decreases rapidly, dropping below 2% when the CO_2 dilution reaches 50%. This change is attributed to two factors. On the one hand, thermal + prompt NO is primarily formed under high-temperature conditions, and the increase in CO_2 content significantly reduces the T_{ad}. On the other hand, CO_2 addition also leads to a reduction in fuel amount under the same ER conditions, resulting in a corresponding decrease in the N_2 concentration in the air. Therefore, the combined effect of these two factors inhibits the formation of thermal + prompt NO.

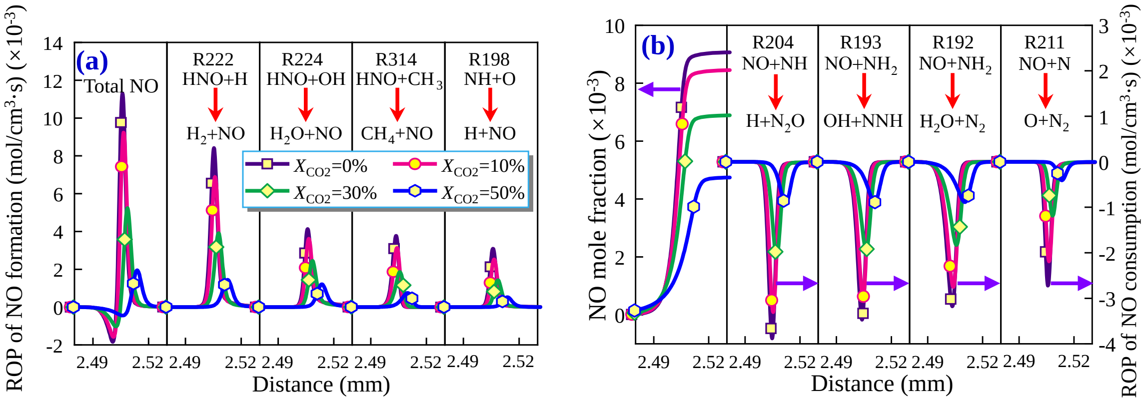

Figure 12. ROP of key elementary reactions involved in NO formation and consumption for varying CO_2 dilution ratios (40% NH_3 + 40% CH_4 + 20% H_2, ER = 0.9, T_0 = 500 K, and P_0 = 5 atm).

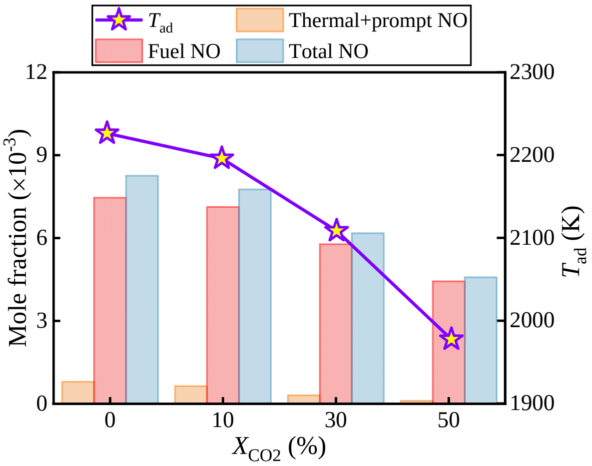

Figure 13. variation in different NO formation sources and Tad for various CO_2 dilution ratios (40% NH_3 + 40% CH_4 + 20% H_2, ER = 0.9, T_0 = 500 K, and P_0 = 5 atm).

4. Conclusions

The LBVs of $NH_3/CH_4/H_2/CO_2$/air premixed flames were measured in a CVCC at different CO_2 additions (0%, 10% and 30%), fuel compositions (40%NH_3 + 40% CH_4 + 20% H_2 and 30%NH_3 + 20% CH_4 + 40% H_2) and ER ranges from 0.6 to 1.3 at T_0 = 500 K and P_0 = 5 atm. The experimental data were accurately predicted using a previously established $NH_3/CH_4/H_2$/CO mechanism. Based on this mechanism, a detailed kinetic simulation was conducted to investigate the effects of different CO_2 dilution ratios and ER on combustion and NO emission. The main conclusions are as follows:

(1) High H_2 and CH_4 content suppresses buoyancy effect. Increasing the CO_2 dilution ratio reduces cracks and cellular structures on the flame surface and enhances propagation speed and stability. Excessive dilution disrupts the spherical flame front and reduces stability.

(2) Increases in X_{CO2} or decreases in H_2 content lead to a reduction in LBV. The dilution of CO_2 inhibits LBV in the following sequence: dilution effect > thermal effect > chemical effect > transport effect. The dilution of CO_2 primarily inhibits LBV by reducing the concentration of O, H, and OH radicals through its dilution effect, particularly under rich-burn conditions. Additionally, increasing CO_2 dilution ratios and ERs enhance the reverse reaction of R21 ($CO + OH = CO_2 + H$), which competes with R1 ($H + O_2 = O + OH$) for H radicals, effectively suppressing the laminar flame propagation.

(3) Increasing the CO_2 dilution ratio reduces NO emissions. The HNO radical contributes most significantly

to NO formation, while NH and NH_2 radicals play key roles in NO reduction. When the CO_2 dilution ratio increases from 0 to 50%, the proportion of thermal + prompt NO drops from 10% to below 2% due to the decrease in adiabatic flame temperature.

Author Contributions: Writing—original draft preparation, W. Z.; Writing—review and editing, W. Z. and X. M.; Validation, W.Z.; Software, W.Z.; Methodology, W.Z.; Conceptualization, X.M., J.T., and W.L.; Visualization, Z.C.; All authors have read and agreed to the published version of the manuscript.

Funding: This research received no external funding.

Institutional Review Board Statement: Not applicable.

Informed Consent Statement: Not applicable.

Data Availability: Statement: Not applicable.

Conflicts of Interest: The authors declare that they have no known competing financial interests or personal relationships that could have appeared to influence the work reported in this paper.

References

1. Li, H.; Zheng, B.; Ciais, P.; Boersma, K.F.; Riess, T.C.V.; Martin, R.V.; Broquet, G.; van der A, R.; Li H.; Hong C. Satellite reveals a steep decline in China's CO_2 emissions in early 2022. *Sci. Adv.* **2023**, *9*, eadg7429. https://doi.org/10.1126/sciadv.adg7429.
2. van der Zwaan, B.; Fattahi, A.; Longa, F.D.; Dekker, M.; van Vuuren, D.; Pietzcker, R.; Rodrigues, R.; Schreyer, F.; Huppmann, D.; Emmerling, J.; et al. Electricity- and hydrogen-driven energy system sector-coupling in net-zero CO_2 emission pathways. *Nat. Commun.* **2025**, *16*, 1368. https://doi.org/10.1038/s41467-025-56365-0.
3. Li, Z.; Wang, K.; Liang, H.; Wang, Y.; Ma, R.; Cao, J.; Huang, L. Marine alternative fuels for shipping decarbonization: Technologies, applications and challenges. *Energy Convers. Manag.* **2025**, *329*, 119641. https://doi.org/10.1016/j.enconman.2025.119641.
4. IMO. 2023 *IMO Strategy on Reduction of GHG Emissions from Ships, Resolution MEPC*; IMO: London, UK, 2023.
5. Zhou, S.; Zhong, W.; Pachiannan, T.; Liu, Q.; Yan, F.; Chen, J.; He, Z.; Wang, Q. Optical Study on Soot Formation of Ethanol/hydrogenated Catalytic Biodiesel/octanol Blends. *Int. J. Automot. Manuf. Mater.* **2023**, *2*, 3. https://doi.org/10.53941/ijamm.2023.100015.
6. Souppez, J.-B.R.; Guttinger, M. Effect of Inlet Diameter on the Temperature of Hydrogen Fuel Tanks for Automotive Applications. *Int. J. Automot. Manuf. Mater.* **2024**, *3*, 1–12. https://doi.org/10.53941/ijamm.2024.100013.
7. LeBlanc, S.; Cong, B.; Sandhu, N.; Jin, L.; Yu, X.; Zheng, M. Combustion Management of Neat Dimethyl Ether Combustion for Enabling High Efficiency and Low NO_x Production. *Int. J. Automot. Manuf. Mater.* **2024**, *3*, 2. https://doi.org/10.53941/ijamm.2024.100020.
8. Zhang, J.; Elbanna, A. M.; Zhu, J.; Qian, Y.; Lu, X. Research on the state-of-the-art of efficient and ultra-clean ammonia combustion: From combustion kinetics to engine applications. *Appl. Energy.* **2025**, *391*, 125886. https://doi.org/10.1016/j.apenergy.2025.125886.
9. Kumar, L.; Sleiti, A.K. Systematic review on ammonia as a sustainable fuel for combustion. *Renew. Sustain. Energy Rev.* **2024**, *202*, 114699. https://doi.org/10.1016/j.rser.2024.114699.
10. Zhu, D.; Shu, B. Recent progress on combustion characteristics of ammonia-based fuel blends and their potential in internal combustion engines. *Int. J. Automot. Manuf. Mater.* **2023**, *2*, 1. https://doi.org/10.53941/ijamm0201001.
11. Erfani, N.; Baharudin, L.; Watson, M. Recent advances and intensifications in Haber-Bosch ammonia synthesis process. *Chem. Eng. Process.-Process Intensif.* **2024**, *204*, 109962. https://doi.org/10.1016/j.cep.2024.109962.
12. Liu, L.; Zhang, M.; Liu, Z. A review of development of natural gas engines. *Int. J. Automot. Manuf. Mater.* **2023**, *2*, 4. https://doi.org/10.53941/ijamm0201004.
13. Okafor, E. C.; Naito, Y.; Colson, S.; Ichikawa, A.; Kudo, T.; Hayakawa A.; Kobayashi H. Measurement and modelling of the laminar burning velocity of methane-ammonia-air flames at high pressures using a reduced reaction mechanism. *Combust. Flame* **2019**, *204*, 162–175. https://doi.org/10.1016/j.combustflame.2019.03.008.
14. Yao, A.; Yao, C. Study of diesel/methanol dual fuel combustion in CI engines and its practice in China. *Int. J. Automot. Manuf. Mater.* **2023**, *2*, 2. https://doi.org/10.53941/ijamm0201002.
15. Lu, M.; Long, W.; Wang, Y.; Wei, F.; Dong, P.; Cong, L.; Tian, H.; Dong, D.; Wang, P.; Wang, Q.; et al. Laminar burning characteristics of ammonia/ methanol mixtures and reaction kinetics analysis at high pressures. *Energy* **2025**, *315*, 134300. https://doi.org/10.1016/j.energy.2024.134300.
16. Xiao, H.; Li, H. Experimental and kinetic modeling study of the laminar burning velocity of NH3/DME/air premixed flames. *Combust. Flame* **2022**, *245*, 112372. https://doi.org/10.1016/j.combustflame.2022.112372.
17. Yu, C.; Guo, L.; Sun, W.; Zhang, H.; Cheng, P.; Yan, Y.; Zhu, G.; Jiang, M.; Guo, Y.; Yue, F. Experimental and chemical kinetic study on effects of H2-DME fusion addition on laminar premixed flame speed and flame instability for ammonia composite combustion. *Energy* **2024**, *310*, 133175. https://doi.org/10.1016/j.energy.2024.133175.
18. Li, H.; Xiao, H. Effect of H2 addition on laminar burning velocity of NH_3/DME blends by experimental and numerical method using a reduced mechanism. *Combust. Flame* **2023**, *257*, 113000. https://doi. org/10.1016/j.combustflame.2023.113000.

19. Berwal, P.; Shawnam; Kumar, S. Laminar burning velocity measurement of CH4/H2/NH3-air premixed flames at high mixture temperatures. *Fuel* **2023**, *331*, 125809. https://doi.org/10.1016/j.fuel.2022.125809.
20. Yasiry, A.; Wang, J.; Zhang, L.; Abdulraheem, A.A.A.; Cai, X.; Huang, Z. An experimental study on H2/NH3/CH4-air laminar propagating spherical flames at elevated pressure and oxygen enrichment. *Int. J. Hydrogen Energy* **2024**, *58*, 28–39. https://doi.org/10.1016/j.ijhydene.2024.01.138.
21. Chu, X.; Li, X.; Gao, P.; Ma, Z.; Xiao, H.; Xie, C.; Zhang, Z.; Wang, X. High-temperature auto-ignition characteristics of NH_3-H_2-CH4. *Fuel* **2024**, *365*, 131228. https://doi.org/10.1016/j.fuel.2024.131228.
22. Bao, L.; Wang, J.; Shi, L.; Chen, H. Exhaust Gas After-Treatment Systems for Gasoline and Diesel Vehicles. *Int. J. Automot. Manuf. Mater.* **2022**, *1*, 9. https://doi.org/10.53941/ijamm0101009.
23. Chen, P.; Wang, H.; Qiao, L.; Gu, M.; Luo, K.; Fan, J. Study of the NO formation characteristics and ammonia-N/coal-N transformation mechanism of ammonia-coal co-combustion in O_2/CO_2 atmosphere. *Combust. Flame* **2024**, *270*, 113756. https://doi.org/10.1016/j.combustflame.2024.113756.
24. Czyzewski, P.; Slefarski, R.; Golebiewski, M.; Alnajideen, M.; Valera-Medina, A. *E*xperimental study of $CO_2/H_2/NH_3$ influence on CH_4 flameless combustion process in semi-industrial furnace. *Energy* **2024**, *296*, 131014. https://doi.org/10.1016/j.energy.2024.131014.
25. Gao, Y.; Li, Y.; Wei, X.; Zheng, Y.; Yang, S.; Yang, Q.; Jiang, H.; Zhang, Y.; Lin, H. A kinetic study of CO_2 and H_2O addition on NO formation for ammonia-methanol combustion. *Fuel* **2025**, *381*, 133283. https://doi.org/10.1016/j.fuel.2024.133283.
26. Alzueta, M.U.; Giménez-López, J.; Mercader, V.D.; Bilbao, R. Conversion of NH3 and NH3-NO mixtures in a CO_2 atmosphere. *A parametric study*, Fuel **2022**, *327*, 125133. https://doi.org/10.1016/j.fuel.2022.125133.
27. Berwal, P.; Khandelwal, B.; Kumar, S. *E*ffect of ammonia addition on laminar burning velocity of CH_4/H_2 premixed flames at high pressure and temperature conditions. *Int. J. Hydrogen Energ*y **2024**, *49*, 112–125. https://doi.org/10.1016/j.ijhydene.2023.06.326.
28. Zhu, W.; Zhang, M.; Zhang, X.; Meng, X.; Long, W.; Bi, M. A comprehensive kinetic modeling study on NH_3/H_2, NH_3/CO NH_3/CH_4 blended fuels. *Int. J. Hydrogen Energy* **2024**, *85*, 228–241. https://doi.org/10.1016/j.ijhydene.2024.08.282.
29. Wu, C. K.; Law, C. K. On the determination of laminar flame speeds from stretched flames. In *Symposium (International) on Combustion*; Elsevier: Amsterdam, The Netherlands, 1985; pp. 1941–1949.
30. Frankel, M.; Sivashinsky, G. On quenching of curved flames. *Combust. Sci. Technol.* **1984**, *40*, 257–268. https://doi.org/10.1080/00102208408923809.
31. Burke, M.P.; Chen, Z.; Ju, Y.; Dryer, F.L. Effect of cylindrical confinement on the determination of laminar flame speeds using outwardly propagating flames. *Combust. Flame* **2009**, *156*, 771 – 779. https://doi. org/10.1016/j.combustflame.2009.01.013.
32. Huang, Z.; Zhang, Y.; Zeng, K.; Liu, B.; Wang, Q.; Jiang, D. Measurements of laminar burning velocities for natural gas–hydrogen–air mixtures. *Combust. Flame* **2006**, *146*, 302–311. https://doi.org/10.1016/j.combustflame.2006.03.003.
33. Wang, P.; Wang, Y.; Lu, M.; Long, W.; Dong, P.; Zhao, W.; Tian, H.; Xiao, G.; Cui, J.; Cao, J. Study on combustion characteristics and analysis method optimization of methanol laminar burning under high pressure and high temperature initial conditions. *Combust. Flame* **2025**, *277*, 114215. https://doi.org/10.1016/j.combustflame.2025.114215.
34. Zhang, Q.; Chen, G.; Deng, H.; Wen, X.; Wang, F.; Zhang, A.; Sheng, W. Experimental and numerical study of the effects of oxygen-enriched air on the laminar burning characteristics of biomass-derived syngas. *Fuel* **2021**, *285*, 119183. https://doi.org/10.1016/j.fuel.2020.119183.
35. Liu, B.; Hu, E.; Yin, G.; Huang, Z. Experimental and kinetic study on laminar burning velocities of ammonia/ethylene/air premixed flames under high temperature and elevated pressure. *Combust. Flame* **2023**, *251*, 112707. https://doi.org/10.1016/j.combustflame.2023.112707.
36. Moffat, R.J. Describing the uncertainties in experimental results. *Exp. Therm. Fluid Sci.* **1988**, *1*, 3–17. https://doi.org/10.1016/0894-1777(88)90043-X.
37. Yu, H.; Han, W.; Santner, J.; Gou, X.; Sohn, C.H.; Ju, Y.; Chen, Z. Radiation-induced uncertainty in laminar flame speed measured from propagating spherical flames. *Combust. Flame* **2014**, *161*, 2815–2824. https://doi.org/10.1016/j.combustflame.2014.05.012.
38. Shrestha, K.P.; Lhuillier, C.; Barbosa ,A.A.; Brequigny, P.; Contino, F.; Mounaïm-Rousselle, C.; Seidel, L.; Mauss, F. An experimental and modeling study of ammonia with enriched oxygen content and ammonia/hydrogen laminar flame speed at elevated pressure and temperature. *Proc. Combust. Inst.* **2021**, *38*, 2163–2174. https://doi.org/10.1016/j.proci.2020.06.197.
39. Zhou, S.; Cui, B.; Yang, W.; Tan, H.; Wang, J.; Dai, H.; Li, L.; Rahman, Z.U.; Wang, X.; Deng, S.; et al. An experimental and kinetic modeling study on NH_3/air, NH_3/H_2/air, NH_3/CO/air, and NH3/CH4/air premixed laminar flames at elevated temperature. *Combust. Flame 2023*, **248**, 112536. https://doi.org/10.1016/j.combustflame.2022.112536.
40. Wang Z.; Han X.; He Y.; Zhu R.; Zhu Y.; Zhou Z.; Cen K. Experimental and kinetic study on the laminar burning velocities of NH_3 mixing with CH3OH and C2H_5OH in premixed flames. *Combust. Flame* **2021**, *229*, 111392. https://doi.org/10.1016/j.combustflame.2021.02.038.
41. Shi, X.; Li, W.; Zhang, J.; Fang, Q.; Zhang, Y.; Xi, Z.; Li, Y. Exploration of NH_3 and NH_3/DME laminar flame propagation in O_2/CO_2 atmosphere: Insights into NH_3/CO_2 interactions. *Combust. Flame* **2024**, *260*, 113245. https://doi.org/10.1016/j.combustflame.2023.113245.
42. Meng, X.; Liu, L.; Qin, M.; Zhu, W.; Long, W.; Bi, M. Modeling and chemical kinetic analysis of methanol and reformed gas (H_2/CO_2) blending with ammonia under lean-burn condition. *Int. J. Hydrogen Energy* **2024**, *58*, 190–

199. https://doi.org/10.1016/j.ijhydene.2024.01.150.

43. Zhu, W.; Zhang, X.; Miao, M.; Meng, X.; Bi, M. Chemical kinetic study of methane blended with ammonia cracked gas at elevated temperature and pressure. *Chem. Eng. J.* **2024**, *498*, 155401. https://doi.org/10.1016/j.cej.2024.155401.
44. Li, S.; Si, J.; Liu, X.; Guo, Y.; Wang, G.; Xu, E.; Zou, J.; Zhang, Q.; Xu, M.; Mi, J. A refined method of identifying NO formation by NH_3 and N_2 for ammonia combustion. *Int. J. Hydrogen Energy* **2025**, *138*, 1004–1016. https://doi.org/10.1016/j.ijhydene.2025.05.206.
45. Alvarez, L.F.; Shaffer, J.; Dumitrescu, C.E.; Askari, O. Laminar burning velocity of Ammonia/Air mixtures at high pressures. *Fuel* **2024**, *363*, 130986. https://doi.org/10.1016/j.fuel.2024.130986.
46. Chen, C.; Wang, Z.; Yu, Z.; Han, X.; He, Y.; Zhu, Y.; Konnov, A.A. Experimental and kinetic modeling study of laminar burning velocity enhancement by ozone additive in $NH_3 + O_2 + N_2$ and $NH_3 + CH_4/C_2H_6/C_3H_8$ + air flames. *Proc. Combust. Inst.* **2023**, *39*, 4237–4246. https://doi.org/10.1016/j.proci.2022.07.025.
47. Xie, M.; Fu, J.; Zhang, Y.; Shu, J.; Ma, Y.; Liu, J.; Zeng, D. Numerical analysis on the effects of CO_2 dilution on the laminar burning velocity of premixed methane/air flame with elevated initial temperature and pressure. *Fuel* **2020**, *264*, 116858. https://doi.org/10.1016/j.fuel.2019.116858.